



HAL
open science

The potential of Pléiades images with high angle of incidence for reconstructing the coastal cliff face in Normandy

Pauline Letortu, Marion Jaud, Claire Théry, Jean Nabucet, Roza Taouki, Sophie Passot, Emmanuel Augereau

► To cite this version:

Pauline Letortu, Marion Jaud, Claire Théry, Jean Nabucet, Roza Taouki, et al.. The potential of Pléiades images with high angle of incidence for reconstructing the coastal cliff face in Normandy. *International Journal of Applied Earth Observation and Geoinformation*, 2020, 84, pp.101976. 10.1016/j.jag.2019.101976 . hal-02281865

HAL Id: hal-02281865

<https://hal.science/hal-02281865>

Submitted on 22 Jan 2020

HAL is a multi-disciplinary open access archive for the deposit and dissemination of scientific research documents, whether they are published or not. The documents may come from teaching and research institutions in France or abroad, or from public or private research centers.

L'archive ouverte pluridisciplinaire **HAL**, est destinée au dépôt et à la diffusion de documents scientifiques de niveau recherche, publiés ou non, émanant des établissements d'enseignement et de recherche français ou étrangers, des laboratoires publics ou privés.

The potential of Pléiades images with high angle of incidence for reconstructing the coastal cliff face in Normandy (France)

Pauline Letortu^{a*}, Marion Jaud^{a,b}, Claire Théry^a, Jean Nabucet^c, Roza Taouki^a, Sophie Passot^d, Emmanuel Augereau^a

^aUniversity of Bretagne Occidentale, IUEM, CNRS, UMR 6554 – LETG, Technopôle Brest-Iroise, rue Dumont d'Urville, Plouzané, 29280, France, pauline.letortu@univ-brest.fr, claire_thery1@hotmail.fr, Roza.Taouki@ensg.eu, emmanuel.augereau@univ-brest.fr

^bUniversity of Bretagne Occidentale, IUEM, CNRS, UMS 3113 – IUEM, Technopôle Brest-Iroise, Rue Dumont d'Urville, Plouzané, 29280, France, marion.jaud@univ-brest.fr

^cUniversity of Rennes 2, CNRS, UMR 6554 – LETG, Place du Recteur Henri Le Moal, Rennes, 35000, France, jean.nabucet@uhb.fr

^dUniversité Claude Bernard Lyon 1, UMR 5276 - Laboratoire de Géologie de Lyon: Terre, Planètes, Environnement, ENS Lyon, Villeurbanne, 69622, France, sophie.passot@univ-lyon1.fr

^eUniversity of Bretagne Occidentale, IUEM, CNRS, UMR 6538 – IUEM, Technopôle Brest-Iroise, Rue Dumont d'Urville, Plouzané, 29280, France

*Corresponding author. Tel.: +33 290915588, pauline.letortu@univ-brest.fr

Abstract

To monitor chalk cliff face along the Normandy coast (NW France) which is prone to erosion, we tested the potential of cliff face 3D reconstruction using pairs of images with high angle of incidence at different dates from the agile Pléiades satellites. The verticality aspect of the cliff face brings difficulties in the 3D reconstruction process. Furthermore, the studied area is challenging mainly because the cliff face is north-oriented (shadow). Pléiades images were acquired over several days (multi-date stereoscopic method) with requested incidence angles until 40°. 3D reconstructions of the cliff face were compared using two software: ASP[®] and ERDAS IMAGINE[®]. Our results are twofold. Firstly, despite ASP[®] provides denser point clouds than ERDAS IMAGINE[®] (an average of 1.60 points/m² from 40° incidence angle stereoscopic pairs on the whole cliff face of Varengueville-sur-Mer against 0.77 points/m² respectively), ERDAS IMAGINE[®] provides more reliable point clouds than ASP[®] (precision assessment on the Varengueville-sur-Mer cliff face of 0.31 m ± 2.53 and 0.39 m ± 4.24 respectively), with a better spatial distribution over the cliff face and a better representation of the cliff face shape. Secondly, the quality of 3D reconstructions depends mostly on the amount of noise from raw images and on the shadow intensity on the cliff face (radiometric quality of images).

Keywords

Pléiades imagery; high incidence angle images; cliff face erosion; 3D reconstruction; Normandy

1. Introduction

Coastal areas have high density populations due to rich resources and good social and recreational infrastructures. This trend is likely to increase with time but with spatial differences (Neumann et al., 2015). About 52% of the global shoreline is made of cliff coasts that can only retreat (Young and Carilli, 2019). The erosion of these coasts could be dramatic, with occasional massive falls which can threaten people, buildings, utilities and infrastructure located near the coastline (Lim et al., 2005; Naylor et al., 2010; Moses and Robinson, 2011; Kennedy et al., 2014; Letortu et al., 2019). Traditionally, the study of cliff coasts involves quantifying the retreat rates of the cliff top (m/year) with 2D data. This diachronic approach (over several decades) is mainly based on vertical aerial photographs more recently using

52 airborne LIDAR data over a significant spatial scale (several tens to hundreds of kilometers)
53 at multi-year intervals (Young, 2018). These average annual retreat rates poorly reflect the
54 erosive dynamics of cliffs, which are characterized by dead time (marine, subaerial,
55 anthropogenic agents weaken the cliff without eroding it) and high points (sudden falls causing
56 cliff retreat). Subsequently, the fall deposit is evacuated by marine action and erosion
57 continues its action on the new cliff face. Scientists have identified the conditions for a better
58 understanding of the regressive dynamics of cliffs (retreat rates, rhythms of evolution,
59 triggering factors of failure). It is necessary to collect 1) 3D data of the cliff face (from the foot
60 to the top of the cliff) to observe all erosion events (2) at high spatial resolution (inframetric) (3)
61 at very high temporal frequency (from seasonal to daily surveys) and (4) over large-scale areas
62 (hydro-sedimentary cell scale for relevant coastal management).

63 While the terrestrial laser scanning and the UAV photogrammetry or terrestrial
64 photogrammetry can meet the first three conditions, the low spatial representativeness of the
65 results is a major constraint (James and Robson, 2012; Letortu et al., 2018; Westoby et al.,
66 2018). The boat-based mobile laser scanning data bring together three of the conditions but
67 the cost and the necessary technical know-how limit the temporal frequency of the surveys
68 (Michoud et al., 2014). Moreover, these methods can be very expensive and need staff on the
69 field. Images from Pléiades satellites launched in 2011 and 2012 could be adequate because
70 these satellites are very agile (they can reach a viewing angle of up to 47° to image the cliff
71 face), the data are at very high spatial resolution (around 0.70 m ground sampling distance at
72 nadir for panchromatic images), with a daily revisit frequency and a swath width of 20 km at
73 nadir (ASTRIUM, 2012; Boissin et al., 2012). The images acquired from a pushbroom scanner
74 may be free (under certain conditions) for research institutes and do not require specific
75 fieldwork.

76 In a context of coastal morphology mapping, satellite imagery has long been used for large-
77 scale 2D studies, enabling to map shoreline/coastline position and to analyze its evolution (e.g.
78 White and El Asmar, 1999; Boak and Turner, 2005; Gardel and Gratiot, 2006). The
79 development of high-resolution agile satellites has opened up new perspectives, especially for
80 3D reconstruction. Many articles have used Pléiades stereoscopic or tri-stereoscopic
81 acquisitions to answer various scientific questions (e.g. de Franchis et al., 2014; Stumpf et al.,
82 2014; Poli et al., 2015) including in coastal environments (AIRBUS, 2015; Collin et al., 2018;
83 Almeida et al., 2019). But, to our knowledge, Pléiades satellite images have never been used
84 in the context of cliff face monitoring which is challenging because it raises four questions:

- 85 - How to collect Pléiades images on a vertical cliff face?
- 86 - How to process these high angle of incidence images?
- 87 - What is the relevance of this data for cliff face 3D reconstruction (sufficient point density on
88 the cliff face to observe structural discontinuities)?
- 89 - What are the favorable acquisition parameters and site characteristics for cliff face surveys
90 (angle of incidence, season, orientation of the coastline, color of the cliff face)?

91 For this study, images were acquired along the Norman coastal cliffs (Seine-Maritime), from
92 Quiberville to Berneval-le-Grand (20 km, north-oriented cliff face) because the risk of erosion
93 is significant. The fast retreat rate of chalk cliffs has reached urban areas and impacted the
94 local use of the beach. Some areas are under expropriation procedures to protect populations
95 (Dieppe) and a fatality occurred in August 2015 in Varengeville-sur-Mer where a shell
96 fisherman died after being buried by tons of rock due to chalk cliff fall. One of the challenges
97 in coastal management is to predict the coastal evolution in order to protect people living in
98 this environment. This challenge can be achieved using relevant, homogeneous and long-term
99 data including these provided by Pléiades imagery.

100 The standard stereoscopic or tri-stereoscopic acquisition which consists, within the same pass
101 of the satellite on its meridian orbit, of acquiring two or three images over the area of interest
102 (front, nadir and back images) is proved unsuitable in our case because of the orientation of
103 the cliff face: the backward viewing image would capture the plateau but not the cliff face
104 making 3D reconstruction impossible. Furthermore, the studied cliff face being a sub-vertical
105 object, a high angle of incidence should be favorable. Thus, we imagined an original acquisition
106 procedure: as the orbital pass position changes daily, a multi-date survey over several
107 consecutive days, with mono-acquisition and a high angle of incidence (across-track), was
108 performed to observe the area at various viewing angles. In order to assess the impact of the
109 angle of incidence, two sets of images were simultaneously requested: one with a pitch
110 imaging angle of 40° and the second one with a pitch imaging angle between 0° and 10°.
111 First, the study area will be described, followed by the methods of acquisition and data
112 processing of images with a high angle of incidence. In a third step, the results of our
113 exploratory research on the relevance of Pléiades data for reconstructing the Norman cliff face
114 and the favorable acquisition parameters and site characteristics will be presented and
115 discussed. Conclusions will be drawn in the final section.

116

117 2. Study area

118 The study area is located in north-western France (01°00'E; 49°55'N), in Normandy (Seine-
119 Maritime), along the Channel. Climatically, the area belongs to the western part of Europe
120 which is particularly exposed to the influences of oceanic low pressures, and thus, to the types
121 of disturbed weather that dominate approximately 2/3 of the year (Pédelaborde, 1958; Trzpit,
122 1970). Geologically, it belongs to the northeastern part of the Parisian Basin (sedimentary),
123 where the Pays de Caux plateau abruptly ends in subvertical coastal cliffs. Cliffs are made of
124 Upper Cretaceous chalk with flints (Pomerol et al., 1987; Mortimore et al., 2004). The altitude
125 range of the cliffs is between 20 m to 100 m with an increase from south-west to north-east,
126 and locally cut by valleys. As shown in Figure 1, these cliffs are mainly white in color, but the
127 sub-vertical cliffs are darkened (brown color) by a bed of clay and sand sediment of the Tertiary
128 Period (Paleogene) between Sainte-Marguerite-sur-Mer and Dieppe, and elsewhere by clay-
129 flint formations above the chalk strata. The average tidal range is 8 m (macrotidal environment).
130 At low tide the foreshore is characterized by a wide shore platform slightly inclined to the sea
131 with a gravel barrier near the cliff foot contact.

132

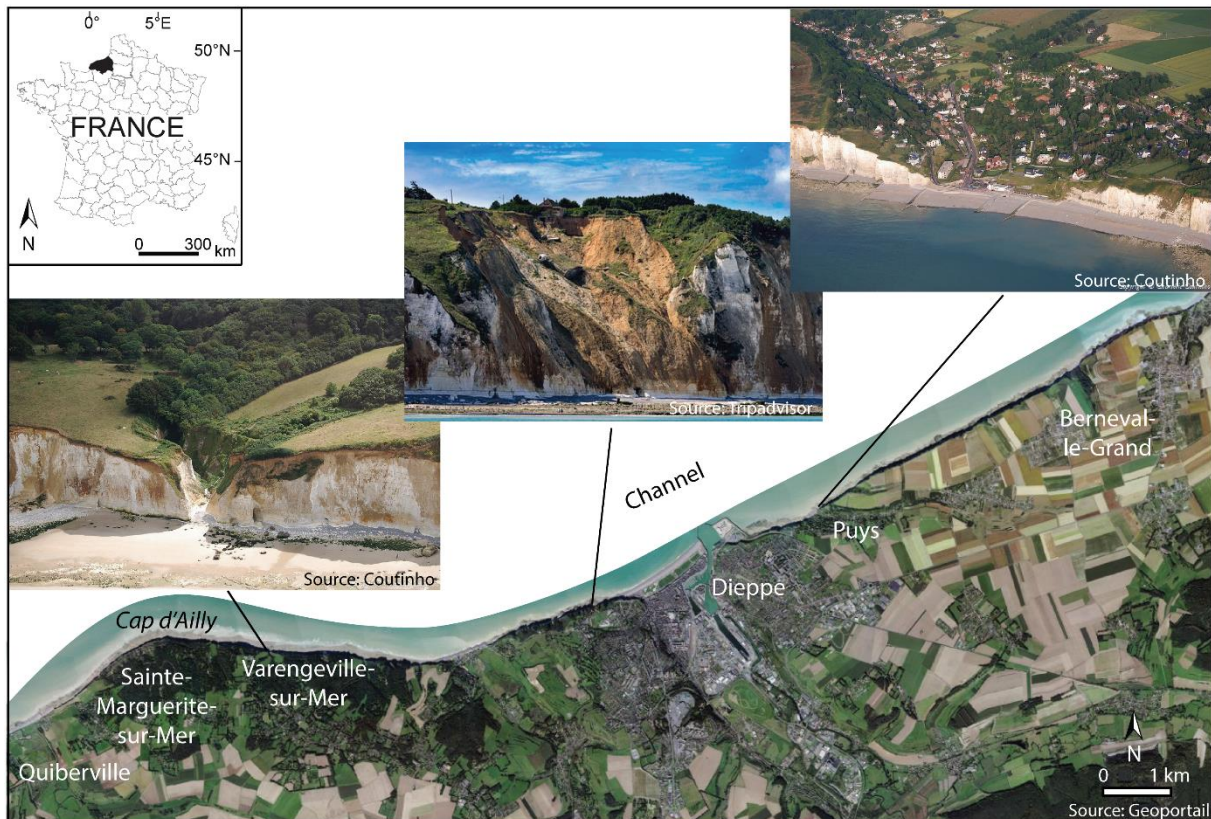


Figure 1 : Presentation of the study area from Quiberville to Berneval-le-Grand (Seine-Maritime, Normandy)

133
134
135

136

137 Along the studied coastline (between Quiberville and Berneval-le-Grand, 20-km long), the
138 lithology of the cliffs from Sainte-Marguerite-sur-Mer to Dieppe is composed of Santonian and
139 Campanian chalk and covered by Paleogene strata. The lithology is prone to erosion with the
140 highest annual retreat rate (0.23 m/year) in comparison with average county retreat rate (0.15
141 m/year between Cap d'Antifer and Le Tréport, 1966-2008 (Letortu et al., 2014)). Between
142 Dieppe and Berneval-le-Grand (Turonian and Coniacian chalk stages), the retreat rate is lower
143 (0.12 m/year). The modalities of erosion are varied with falls of a few m³ to hundreds of
144 thousands of m³ but they are ubiquitous along the cliff line.

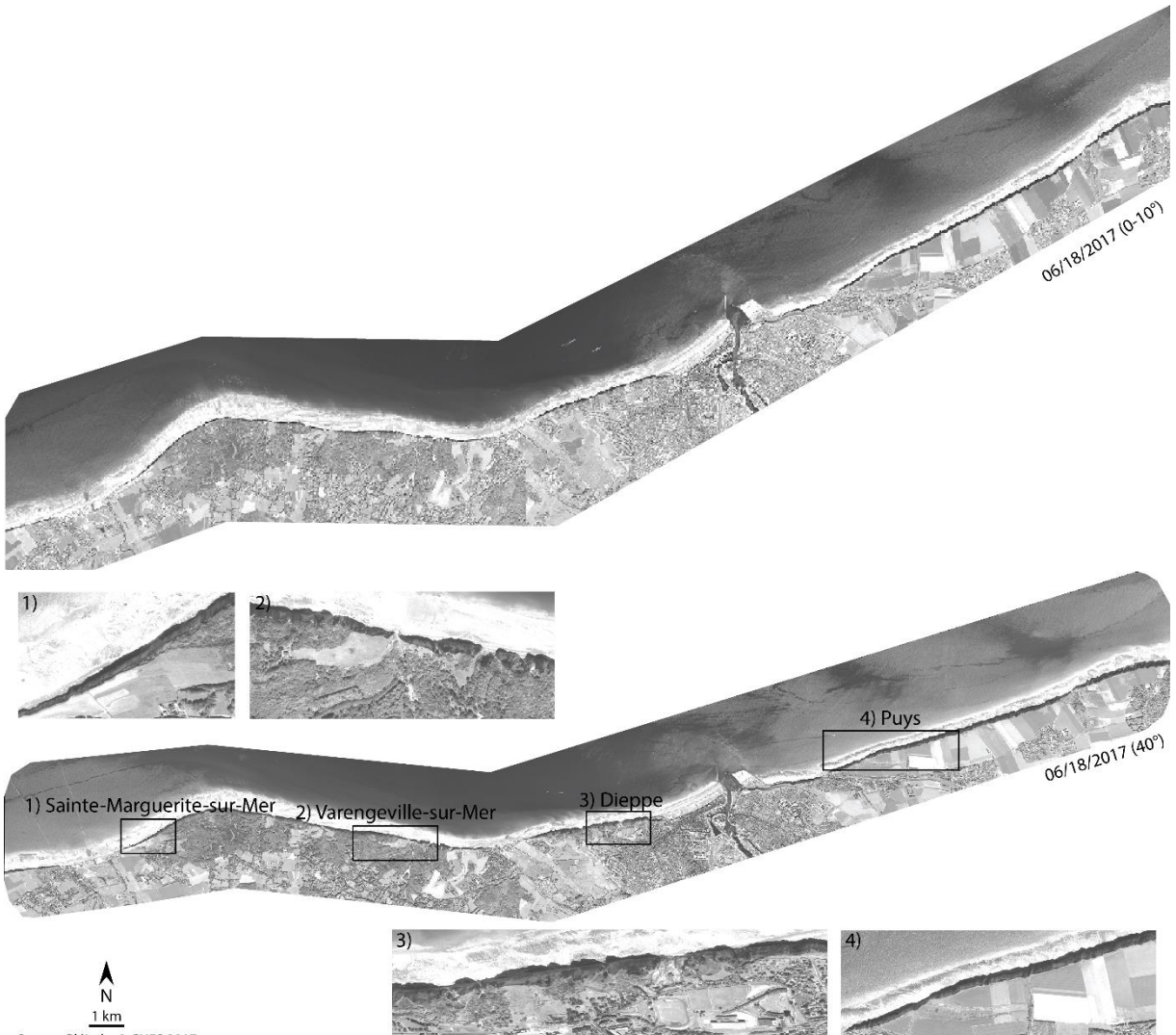
145 The study area is challenging for the acquisition of these satellite images because (1) the
146 SW/NE orientation of the coastline complicates the image acquisition while the Pléiades orbit
147 is meridian; (2) the cliff face is north-oriented, so in the cast shadow during the satellite passing
148 time, even in summer; (3) the weather conditions are often cloudy and rainy in the area
149 because it is located in mid-latitudes where disturbed weather dominates; (4) a high tidal range
150 limits the acquisition periods because the whole cliff face is needed.

151 For the 3D reconstruction, the diversity of cliff types along the 20 km cliff line is also challenging.
152 To assess the quality of reconstructions in function of the site characteristics, four areas of
153 interest (AOIs) were selected: Sainte-Marguerite-sur-Mer, Varengeville-sur-Mer, Dieppe and
154 Puys (Table 1, Figure 2). The whitest cliff faces are located at Puys. The cliff face colors at
155 Sainte-Marguerite-sur-Mer, Varengeville-sur-Mer and Dieppe are from brown to light gray. The
156 shore platform is gray or beige and mainly rocky with gravel accumulation except at Puys,
157 where there are no gravel accumulations. Sainte-Marguerite-sur-Mer and Varengeville-sur-
158 Mer have the lowest cliff height (from 20 to 40 m), with the gentlest cliff face slope at Sainte-
159 Marguerite-sur-Mer (70°). Sainte-Marguerite-sur-Mer and Puys have a sublinear coastline

160 (average depth of incisions from 10 to 20 m) whereas Varengeville-sur-Mer and Dieppe have
 161 a jagged coastline (incisions from 75 to 115 m-deep) (Figure 2).
 162

Area of interest (AOI)	Sainte-Marguerite-sur-Mer (00°56'37"E; 49°54'42"N)	Varengeville-sur-Mer (01°00'22"E; 49°55'01"N)	Dieppe (01°03'33"E; 49°55'27"N)	Puys (01°07'26"E; 49°56'38"N)
Cliff face color	Ochre and light gray	Brown and light gray	Brown and light gray	Light gray
Shore platform color	Dark gray	Beige	Dark gray	Light gray
Type of platform	Rocky and gravel accumulation	Rocky and gravel accumulation	Rocky and gravel accumulation	Rocky
Average cliff height (m)	20-50	30-40	60	70
Average cliff face slope (°)	70	70-90	80-85	80-90
Orientation of cliff face	NW	NNE	NNW	NNW
Average depth of incision* (m)	10	115	75	20

163 Table 1: Main characteristics of the AOI sites (*the depth of incision is the length from the headland to
 164 the trough (perpendicular to the coastline))



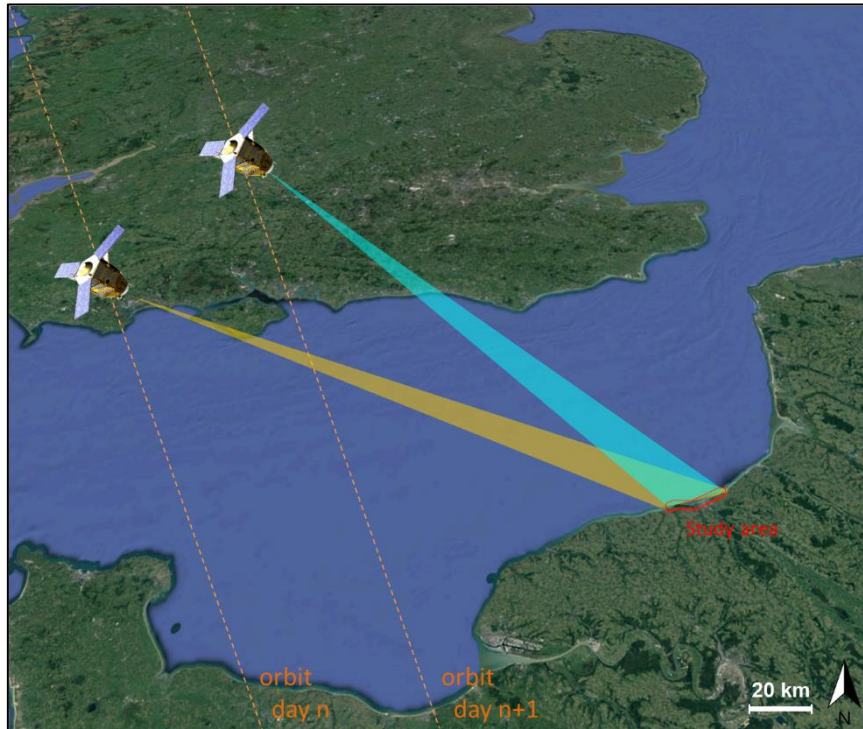
165 Source: Pléiades© CNES 2017
 166 Figure 2: Images acquired on 06/18/2017 with both requested incidence angles and the location of
 167 AOIs

168
169
170
171
172
173
174
175

3. Data collection and processing

3.1. Acquisition strategy

The high angle of incidence needed for the images of the multi-date survey requires the satellite position at the time of acquisition to be above the Channel or the United Kingdom (Figure 3). This means that cloud cover must be from zero to low over large areas, around 11:25 UTC (satellite pass time).



176
177

Figure 3: Principle of the multi-date survey used in this study

178 In this configuration, the acquisition is considered challenging by the image supplier due to the
179 high incidence angle, repetitiveness and short periods of time when the site is accessible under
180 good conditions (zero or low cloud cover (between 0 and 10%) and during low tide if possible).
181

3.2. Acquired images and stereo-pairs

In order to follow the evolution of the studied cliffs, different periods were chosen for Pléiades image acquisition:

- 185 - Fall 2016: 4 stereoscopic pairs;
- 186 - Summer 2017: 5 stereoscopic pairs (Figure 2);
- 187 - Winter 2017/2018: 5 stereoscopic pairs.

188 The angle of incidence is different from the viewing angle due to the sphericity of the Earth. To
189 limit the differences induced by the geometric configuration of the images, we chose to perform
190 3D reconstruction from images acquired with similar incidence angles (either 40° or 0-10°).
191 The images acquired (Table 2) used in this paper are panchromatic ones, as spatial resolution
192 is finer (0.7 m) than multispectral images (2.8 m). However, due to the geometry of acquisition,
193 the ground sampling distance is variable from one day to another, varying for example from
194 0.27 m to 1.83 m for images at 40° of incidence.

195

Date	Hour (UTC)	Name of satellite	Requested incidence angle	Weather	Pitch viewing angle (°)	Roll viewing angle (°)	Pitch incidence angle (°)	Roll incidence angle (°)	Oblique distance between the satellite and the cliff (m)
10/05/2016	11:29	1B	0-10	Sunny	2.25	29.16	12,96	-3.01	707856
10/06/2016	11:21	1A	0-10	Cloudy	4.78	20.75	-11.50	-21.13	727351
10/08/2016	11:06	1A	0-10	Sunny	-0.7	0.9	0.74	-1.16	694160
10/31/2016	11:29	1B	0-10	Sunny	-1.06	29.28	-9.49	-31.98	700857
06/10/2017	11:21	1B	0-10	Sunny	9.65	20.6	-16.56	-19.65	743652
06/15/2017	11:33	1B	0-10	Sunny	1.01	32.83	-11.75	-35.9	703506
06/18/2017	11:10	1A	0-10	Sunny	3.07	6.47	-4.6	-5.39	698687
07/06/2017	11:21	1B	0-10	Cloudy	9.13	20.45	-15.95	-19.64	742090
07/21/2017	11:06	1A	0-10	Sunny	9.71	0.17	-10.4	2.2	916552
12/01/2017	11:32	1A	0-10	Cloudy	30.47	31.29	-11.75	-35.86	884638
12/16/2017	11:17	1B	0-10	Cloudy	9.71	15.72	-14.78	-14.35	759203
01/24/2018	11:17	1A	0-10	Cloudy	-0.66	16.09	-3.88	-17.54	731573
02/12/2018	11:20	1A	0-10	Cloudy	9.15	20.34	-15.93	-19.51	742410
02/17/2018	11:32	1A	0-10	Sunny	5.91	32.44	-18.71	-33.79	720932
10/05/2016	11:27	1B	40	Sunny	40.65	26.65	-50.56	-15.94	1023748
10/06/2016	11:20	1A	40	Cloudy	30.39	19.35	-37.59	-11.93	884387
10/08/2016	11:05	1A	40	Cloudy	34,15	0.7	-37.55	10.79	850050
10/31/2016	11:28	1B	40	Misty	30.39	27.7	-40.49	-21.52	878726
06/10/2017	11:20	1B	40	Sunny	40.69	18.35	-48.5	-6.23	1026143
06/15/2017	11:31	1B	40	Sunny	30.48	31.32	-42.09	-25.81	884838
06/18/2017	11:08	1A	40	Sunny	37.32	3.83	-41.92	7.65	890433
07/06/2017	11:20	1B	40	Sunny	30.46	19.22	-37.62	-11.77	885380
07/21/2017	11:05	1A	40	Sunny with scattered clouds	39.24	1.42	-43.56	13.63	704437
12/01/2017	11:31	1A	40	Cloudy	-1.03	32.79	-42.08	-25.74	703402
12/16/2017	11:17	1B	40	Cloudy	30.43	14.5	-36.34	-6.6	896286
01/24/2018	11:16	1A	40	Cloudy	30.48	14.46	-36.38	-6.57	896897
02/12/2018	11:20	1A	40	Cloudy	30.46	19.11	-37.59	-11.67	885643
02/17/2018	11:30	1A	40	Sunny	36.03	30.63	-47.2	-22.92	954538

Table 2: Characteristics of acquired Pléiades images

196

197

198 For the 3D reconstruction of the cliff face, the 0-10° and 40° images were examined according
199 to three criteria to select the stereoscopic pairs which appeared relevant to process:

200 - The absence of rock falls between both images: Thus, a study of falls on the AOIs between
201 2016 and 2018 identified one fall at Varengeville-sur-Mer on 10/23/2017, two falls at Sainte-
202 Marguerite-sur-Mer (one between 07/21/2017 and 12/12/2017, the other between 07/21/2017
203 and 12/01/2018), one fall at Puys (between 01/24/2018 and 02/12/2018). It is possible that
204 some falls were missed, therefore it was decided that the acquisition period for stereoscopic
205 image pairs should not exceed 2 months;

206 - Good image quality: A clear sky is required between the satellite and the study area to have
207 a cloud-free imagery (Berthier et al., 2014), thus a satisfactory radiometric quality. This
208 statement is also true for the cliff shadow. In our study area, a good radiometric quality (values
209 of the pixels vary from 0 to 4095 for 12 bit images) is between 134 and 827 for the mean value
210 and between 177 and 1543 for the standard deviation. Meteorology and the size of the shadow
211 on the cliff face have been grouped together under the parameter "visual image evaluation".
212 Only images with good visual image evaluation were retained.

213 - The "flattening" coefficient of the pixels must be limited: where pixel flattening
214 coefficient=Image resolution (x)/Image resolution (y). In our study, flattening coefficient has to
215 be between 0.22 and 2.23 to facilitate feature recognition between images. Not surprisingly,

216 the flattening of the pixels is much less marked at 0-10° than at 40° (on average 0.92 at 0-
 217 10° and 0.55 at 40°).
 218 Taking into account these three criteria, 23 image pairs were tested (Table 3).

219

Date of stereoscopic pairs		Incidence angles (°)
06/10/2017	06/15/2017	0-10
06/15/2017	07/06/2017	0-10
12/01/2017	12/16/2017	0-10
01/24/2018	02/12/2018	0-10
01/24/2018	02/17/2018	0-10
02/12/2018	02/17/2018	0-10
10/05/2016	10/08/2016	40
10/05/2016	10/31/2016	40
10/08/2016	10/31/2016	40
06/10/2017	06/15/2017	40
06/10/2017	06/18/2017	40
06/10/2017	07/06/2017	40
06/15/2017	06/18/2017	40
06/15/2017	07/06/2017	40
06/15/2017	07/21/2017	40
06/18/2017	07/06/2017	40
06/18/2017	07/21/2017	40
07/06/2017	07/21/2017	40
12/01/2017	12/16/2017	40
12/01/2017	01/24/2018	40
01/24/2018	02/12/2018	40
01/24/2018	02/17/2018	40
02/12/2018	02/17/2018	40

220 Table 3: Stereoscopic pairs used for data processing

221 3.3. Data processing

222 Usually, different software (commercial and open-source) can be used for 3D reconstruction
 223 but, in our case, the unusual configuration of images may restrict the choice of suitable
 224 software.

225 In this study, an open-source (ASP® 3.5.1) and a commercial software (ERDAS IMAGINE®)
 226 were used. ERDAS IMAGINE® is a commercial software suite for the creation, visualization,
 227 geocorrection, reprojection and compression of geospatial data. ASP® (Ames Stereo Pipelines,
 228 NASA) is a suite of free and open-source automated geodesy and stereogrammetry tools
 229 (Shean et al., 2016) notably developed for satellite imagery with very detailed documentation
 230 (NASA, 2019, <https://ti.arc.nasa.gov/tech/asr/groups/intelligent-robotics/ngt/stereo/#Documentation>).

231
 232 Internal and external parameters of the pushbroom sensor are provided with each image. They
 233 are empirically described using rational polynomial camera model. Images are provided with
 234 Rational Polynomial Coefficients (RPCs), approximating functions which describe the
 235 relationship between image space and object space (de Franchis et al., 2014). RPCs are
 236 accurate only within a specified validity zone and can reveal inconsistencies for large scenes
 237 and/or multi-temporal acquisitions (Rupnik et al., 2016). Both ERDAS IMAGINE® and ASP®
 238 use RPC sensor model to perform orthorectification and georectification. For some processing
 239 chains, RPCs are computed or affined using Ground Control Points (GCPs) collected

240 throughout the area (Salvini et al., 2004; Kotov et al., 2017). In our case, no GCPs were used
241 and the RPC-based sensor orientation was only refined using tie points identified on both
242 images of the pair.

243 In ERDAS IMAGINE[®], automatic tie point detection provided poor results probably due to high
244 incidence angles and multi-date images. To improve detection, we manually pointed tie points
245 on each image. A minimum of 25 points was chosen (optimal threshold defined after trials
246 between availability of relevant tie points and quality of Root Mean Square Error (RMSE)).
247 These points are preferably identifiable and unchangeable elements on flat areas, where
248 distortions are limited (middle of a crossroads rather than a house roof). In addition, tie points
249 are mainly located near the coast in order to minimize correlation errors over this area of
250 interest. A polynomial model is considered satisfactory when all the points have a RMSE
251 inferior to 0.5 pixels (Vanderstraete et al., 2003). When the RMSE of the triangulation ratio was
252 greater than 0.5 pixels or when the uncertainty threshold was greater than 4 meters for a tie
253 point, it was systematically removed and replaced by a better point. In ASP[®], we skipped this
254 step because co-registration using a rigid-body transformation can accomplish similar results
255 with reduced processing time (Shean et al., 2016).

256 Epipolar images are then computed to perform stereo-matching in both software (Normalized
257 Cross Correlation algorithm in ERDAS IMAGINE[®], More Global Matching (MGM) one in ASP[®]).
258 This stereo-matching step consists of cross-correlation to identify pixel correspondences
259 between the left and right epipolar images. Given characteristic variations of the stereoscopic
260 pairs (multi-date), it is difficult to standardize the processing parameters within the software
261 and between software. As the areas of interest correspond to steep slopes, we used small
262 correlation windows (7*7 pixels, 9*9 pixels). The small size of the windows may introduce more
263 false matches or noise (NASA, 2019). Because of the shadow on the cliff face, the "low contrast"
264 parameter was activated in ERDAS IMAGINE[®] during the image matching to force it to find tie
265 points in this area. In ASP[®], the MGM algorithm was used to decrease high frequency artifacts
266 in low texture areas in order to find more corresponding pixels between both images.

267 Sub-pixel refinement was used in ERDAS IMAGINE[®] (Least Square Refinement) whereas it
268 was not used in ASP[®] in order to reduce processing time (Shean et al., 2016) without altering
269 quality of our results.

270 In ASP[®], we used post filtering to filter disparity (artifacts) with three filters: median-filter-size
271 (3 pixels), texture-smooth-size (11 pixels) and texture-smooth-scale (0.15 pixels).

272 Finally, a 3D position can be computed for each pair of corresponding pixels. The software
273 also generate a DEM, but considering the verticality of the cliff face, we only exported the 3D
274 point cloud.

275 The point clouds are then post-processed with CloudCompare[®], an open-source software, to
276 manually filter artifacts in the point cloud.

277 To assess the impact of the study site characteristics and of the acquisition parameters, the
278 parameterization of both software was not changed from one stereoscopic pair to another or
279 from one AOI to another.

280

281 4. Results and discussion

282 4.1. Comparison of the results provided by the different processing

283 4.1.1. Point density

284 In order to have a relevant cliff face monitoring, it is necessary that the whole cliff face is
285 sampled during 3D reconstruction with sufficient resolution to observe the structural
286 discontinuities of the cliff face. The average density of the point clouds corresponding to the
287 Varengeville-sur-Mer cliff face is calculated (Table 4). The point density is much higher for 3D

288 reconstructions made with ASP® than ERDAS IMAGINE® (respectively, 1.86 points/m² versus
 289 0.24 points/m² on the whole cliff face for 0-10° of incidence angle and 1.60 points/m² versus
 290 0.77 points/m² for 40° of incidence angle). Regardless of the angle of the images and the used
 291 software, the cliff foot is the least densely reconstructed part (0.74 points/m² with ASP® and
 292 0.04 points/m² with ERDAS IMAGINE® for a pair of images at 0-10°) while the most
 293 reconstructed part is the cliff top (1.37 points/m² with ASP® and 0.89 points/m² with ERDAS
 294 IMAGINE® for a pair of images at 40°). This point density difference might be due to the
 295 correlation step using different algorithms.
 296

Location on the cliff face	Requested incidence angles used for 3D reconstruction	Average point density (number of points/m ²) with ASP®	Average point density (number of points/m ²) with ERDAS IMAGINE®
Cliff top	0-10°	1.87	0.15
	40°	1.37	0.89
Middle of the cliff face	0-10°	1.64	0.13
	40°	1.45	0.67
Cliff foot	0-10°	0.74	0.04
	40°	1.03	0.25
Whole cliff face	0-10°	1.86	0.24
	40°	1.60	0.77

297 Table 4: Average density of the point clouds in Varengeville-sur-Mer in function of the cliff face part
 298 and the used software

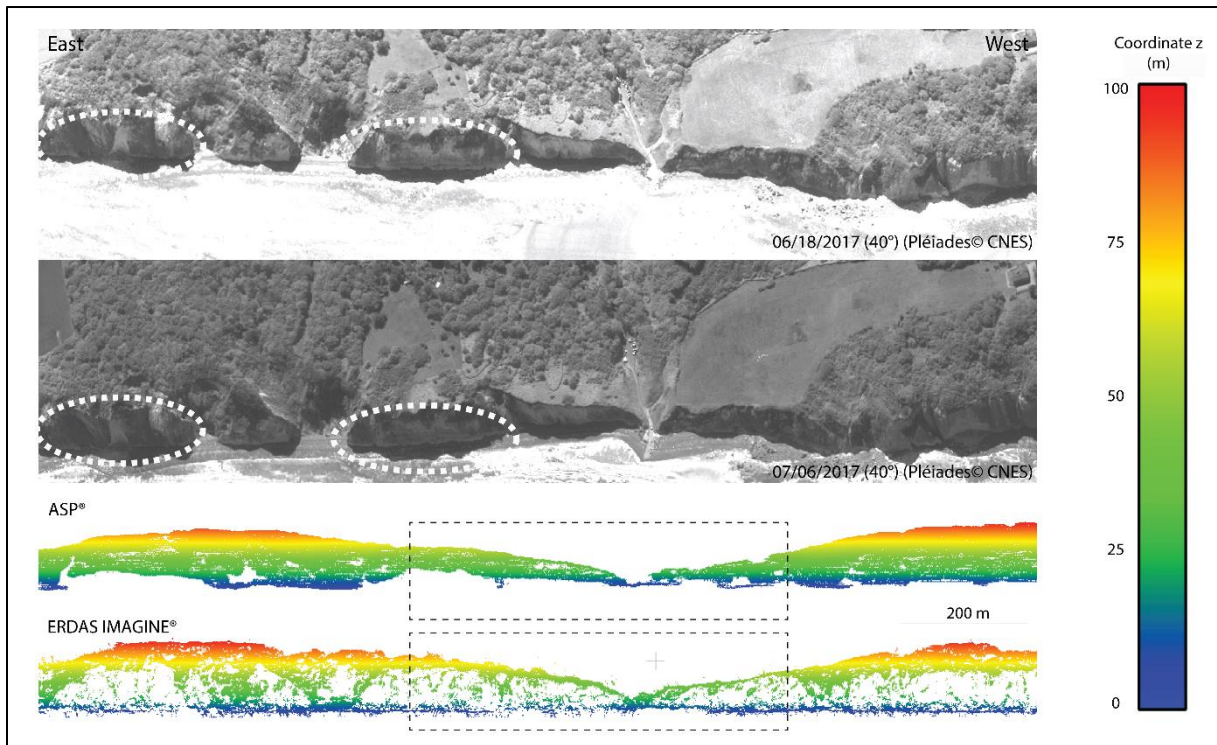
299
 300 *4.1.2. Point distribution*

301 The point distribution of the 3D reconstructions obtained on the cliff face with both software is
 302 different (Figure 4). Although the point cloud obtained with ASP® is denser than that obtained
 303 with ERDAS IMAGINE®, the shape of the cliff is more realistic with ERDAS IMAGINE® (see
 304 dotted black frames in Figure 4).

305 With ASP®, there are very few artifacts on the plateau and on the platform. They are mainly
 306 located on edges of the point cloud and at shadow/sunlit contact (white dotted circles depict
 307 areas where the contact is located about 20 m from the foot of the cliff (Figure 4)). At this latter
 308 area, artifacts have the shape of a stair step.

309 For ERDAS, there are spike-shaped artifacts on the plateau but also on the platform because
 310 the optimization of processing parameters is focused on the cliff face and is not suitable for the
 311 whole area. These artifacts make cleaning difficult. In the shadow/sunlit contact, the points are
 312 higher than the rest of the points on the platform.

313 The 3D reconstruction obtained with ASP® was filtered (data deleted in post-processing with
 314 CloudCompare®) in the circles because of an unrealistic stair-step artifact. The 3D
 315 reconstruction from ERDAS IMAGINE® is not very dense within the circles, but the few
 316 scattered points allow realistic observation of the cliff foot (Figure 4).
 317



318
 319 Figure 4: Distribution of points of the reconstructed cliff faces from the stereoscopic pair on 06/18/2017
 320 and 07/06/2017 with a requested incidence angle of 40° at Varengeville-sur-Mer. The white dotted
 321 circles depict areas where the shadow/sunlit contact is located about 20 m from the foot of the cliff, thus
 322 where reconstruction is challenging.

323

324 **4.1.3. Planimetric precision assessment**

325 To georeference the point clouds from Pléiades images and compare them to multi-source
 326 data (UAV, TLS...), we proceeded to a semi-automatic co-registration using a rigid-body
 327 transform. This co-registration is efficiently constrained vertically (shore platform, plateau) and
 328 alongshore. Thus, precision error is assessed in the cross-shore direction (which is the
 329 direction of erosion on the cliff face).

330 The precision assessment is performed on the AOI of Varengeville-sur-Mer because UAV data
 331 were acquired on 06/26/2017 (by Azur Drones Company for RICOCHET research project).
 332 The precision assessment is based on the relative distance (normal of the cliff face) after fitting
 333 (Iterative Closest Point algorithm in Cloudcompare®) between the 3D point cloud reconstructed
 334 from Pléiades images (11 stereoscopic pairs in June and July 2017) and the one from UAV
 335 images (model). These synchronous surveys allow to limit errors due to erosion events. Table
 336 5 summarizes the relative precision of the cliff face reconstructions.

337

Date of stereoscopic pairs		Requested incidence angle used for 3D reconstruction	Average relative distance (normal of cliff face) [standard deviation] with ASP®	Average relative distance (normal of cliff face) [standard deviation] with ERDAS IMAGINE®
06/10/2017	06/15/2017	0-10°	0.10 [4.94]	0.45 [2.69]
06/15/2017	07/06/2017	0-10°	0.05 [4.45]	0.06 [2.34]
06/10/2017	06/15/2017	40°	0.76 [3.88]	0.43 [3.04]
06/10/2017	06/18/2017	40°	0.26 [3.55]	0.83 [2.47]

06/10/2017	07/06/2017	40°	-0.23 [3.59]	0.00 [2.81]
06/15/2017	07/21/2017	40°	0.89 [4.99]	0.62 [2.85]
06/15/2017	06/18/2017	40°	-0.01 [4.02]	0.57 [2.44]
06/15/2017	07/06/2017	40°	0.17 [4.62]	-0.09 [2.11]
06/18/2017	07/06/2017	40°	1.03 [4.04]	0.25 [1.86]
06/18/2017	07/21/2017	40°	1.23 [4.65]	-0.37 [2.82]
07/06/2017	07/21/2017	40°	0.07 [3.89]	0.63 [2.39]
Average relative distance (normal of cliff face) for the 11 stereoscopic pairs [average standard deviation]			0.39 [4.24]	0.31 [2.53]

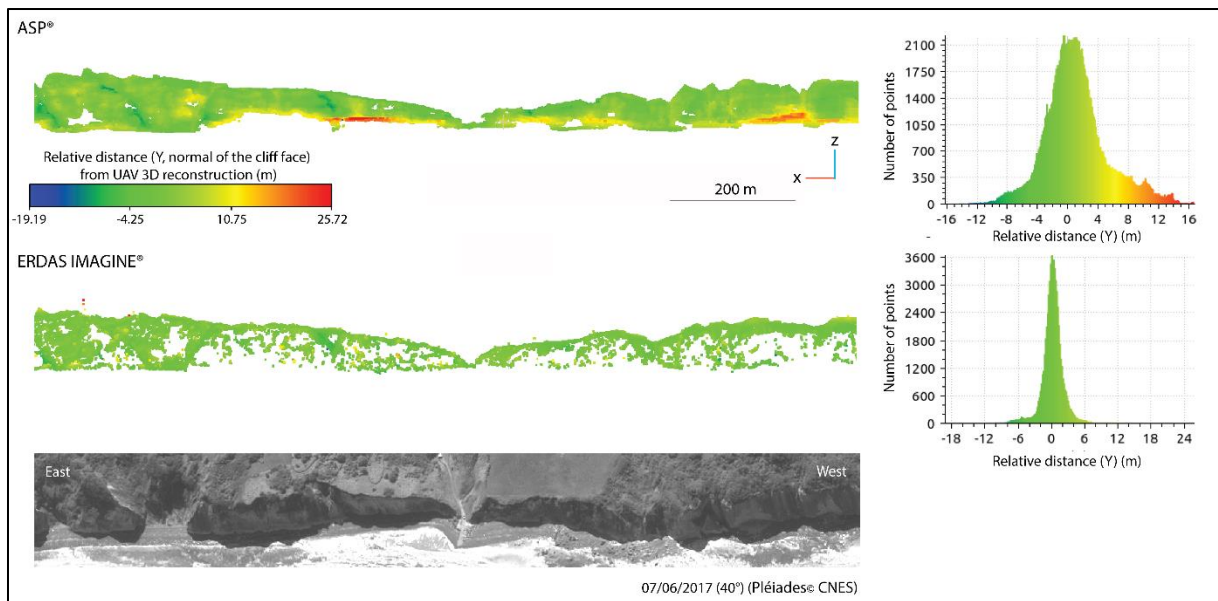
338 Table 5: Relative distance of cliff face normal at Varengeville-sur-Mer between 3D reconstruction from
339 Pléiades images (stereoscopic pairs in June and July 2017) and the one from UAV images
340 (06/26/2017)

341 The precision of the cliff face reconstruction is slightly better with ERDAS IMAGINE® than ASP®
342 (average relative distance of 0.31 m and 0.39 m respectively). Furthermore, the standard
343 deviations are lower with ERDAS IMAGINE® than with ASP® (average standard deviation of
344 2.53 and 4.24 m respectively). With a better average precision associated with a low error
345 dispersion on the cliff face, the 3D reconstruction with ERDAS IMAGINE® provides a reliable
346 dataset. Nevertheless, these better results in precision can partly originate from lower point
347 density of the ERDAS® point clouds than of ASP® point clouds.

348 Regardless of the processing software used, the precision of the cliff face reconstruction is
349 better for acquisitions with a 0-10° incidence angle than with a 40° angle. Indeed, low angles
350 of incidence can limit distortions and inaccuracies of the RPC-based sensor orientation.

351 The spatial distribution of the relative distance between cliff face reconstruction and UAV data
352 is different in function of the software (Figure 5). The 3D reconstruction obtained with ASP®
353 creates a difference of more than 10 m at the foot of the cliff, where an artifact in the shape of
354 a stair step appears because of the shadow. Concerning the 3D reconstruction obtained with
355 ERDAS IMAGINE®, the large differences (greater than 6 m) are scarce and mainly randomly
356 distributed over the whole cliff face. These artifacts can be removed by manual filtering.

357



358
359
360
361

Figure 5: Relative distance of the cliff face normal (in m) at Varengueville-sur-Mer between 3D reconstructions with ERDAS IMAGINE® and ASP® (stereoscopic pair on 06/18/2017 and 07/06/2017 acquired at 40° requested incidence angle) in comparison with UAV data (06/26/2017)

362
363
364
365
366

In our study, despite a higher point density of the ASP® reconstruction compared to ERDAS IMAGINE® one, the latter software is more suitable because the reconstructed points are more precise and better distributed over the cliff face, providing a reliable dataset.

367
368
369
370
371
372
373
374
375
376
377

4.2. Identification of image pairs which give satisfactory reconstruction of the cliff face

First of all, the quality of 3D reconstruction of the cliff face proved to be less relevant than expected. Based on the point resolution on the cliff face, many couples have "unusable" reconstructions with very few points on the cliff face (< 1 pt/30 m) and/or with a proportion of computational artifacts greater than or equal to the proportion of valid points. Computational artifacts can be due to unsuitable geometry of acquisition between the images of the couple or bad tie point detection during correlation. Thus, for "usable" 3D reconstructions, less restrictive thresholds have been put in place:

- "few satisfactory" when the density is < 1 pt/15 m but a good signal to noise ratio;
- "satisfactory" when the density is > 1 pt/15 m (Figure 6).

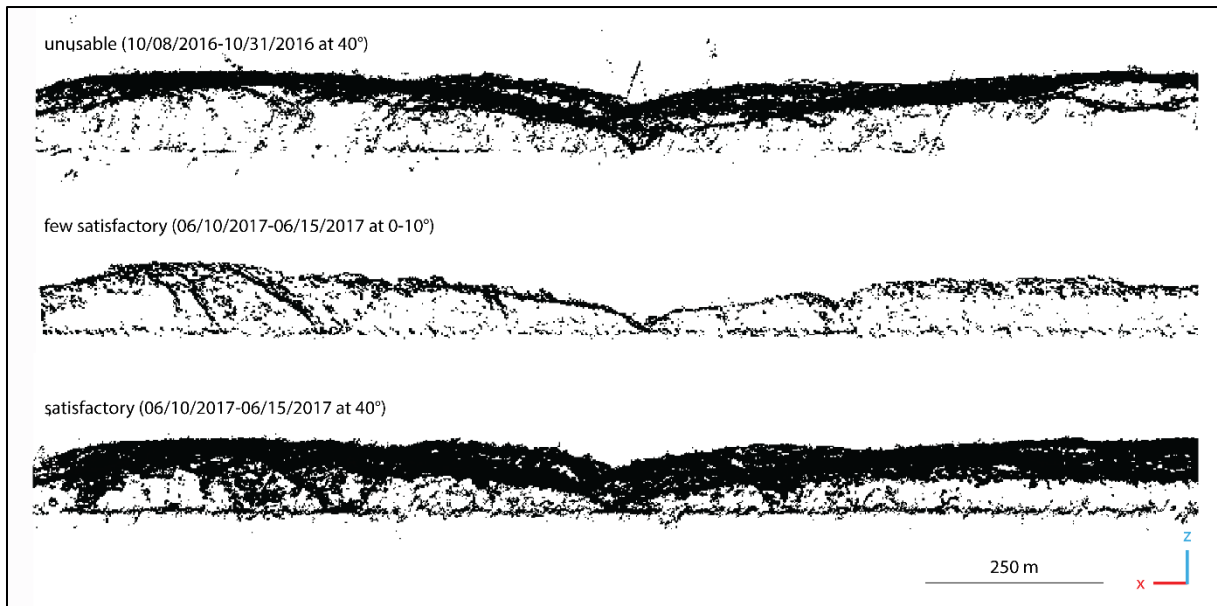


Figure 6: Ranking of 3D reconstruction quality of the cliff face in Varengeville-sur-Mer

378
379
380
381
382
383
384

The last threshold allows visibility of structural discontinuities from the cliff foot to the cliff top. Since ERDAS IMAGINE® creates reliable 3D reconstruction, this software is used to sort the different image pairs on the different AOI (Table 6).

Image 1	Image 2	Set of images (°)	Sainte-Marguerite-sur-Mer	Varengeville-sur-Mer	Dieppe	Puys
06/10/2017	06/15/2017	0-10	few satisfactory	few satisfactory	satisfactory	satisfactory
06/15/2017	07/06/2017	0-10	few satisfactory	satisfactory	satisfactory	satisfactory
12/01/2017	12/16/2017	0-10	unusable	unusable	unusable	unusable
01/24/2018	02/12/2018	0-10	unusable	unusable	unusable	few satisfactory
01/24/2018	02/17/2018	0-10	unusable	unusable	unusable	unusable
02/12/2018	02/17/2018	0-10	unusable	unusable	unusable	unusable
10/05/2016	10/08/2016	40	unusable	unusable	unusable	unusable
10/05/2016	10/31/2016	40	unusable	unusable	unusable	unusable
10/08/2016	10/31/2016	40	few satisfactory	unusable	unusable	unusable
06/10/2017	06/15/2017	40	few satisfactory	satisfactory	satisfactory	few satisfactory
06/10/2017	06/18/2017	40	satisfactory	satisfactory	satisfactory	satisfactory
06/10/2017	07/06/2017	40	few satisfactory	satisfactory	satisfactory	satisfactory
06/15/2017	06/18/2017	40	few satisfactory	satisfactory	satisfactory	few satisfactory
06/15/2017	07/21/2017	40	few satisfactory	satisfactory	unusable	unusable
06/15/2017	07/06/2017	40	satisfactory	satisfactory	satisfactory	satisfactory
06/18/2017	07/06/2017	40	few satisfactory	satisfactory	satisfactory	satisfactory
06/18/2017	07/21/2017	40	satisfactory	satisfactory	unusable	unusable
07/06/2017	07/21/2017	40	unusable	satisfactory	satisfactory	unusable
12/01/2017	12/16/2017	40	unusable	unusable	unusable	unusable

12/01/2017	01/24/2018	40	unusable	unusable	few satisfactory	unusable
01/24/2018	02/12/2018	40	unusable	unusable	unusable	unusable
01/24/2018	02/17/2018	40	unusable	unusable	satisfactory	unusable
02/12/2018	02/17/2018	40	unusable	unusable	unusable	unusable

Table 6: Quality of cliff face 3D reconstructions on ERDAS IMAGINE® in function of the 23 stereoscopic pairs

385
386

387 On the 92 tests, 29 give satisfactory 3D reconstruction (as in Figures 4 and 5), 13 are few
388 satisfactory and the rest is unusable. Stereoscopic pairs at 40° provide more satisfactory 3D
389 reconstruction over the four AOIs than stereoscopic pairs at 0-10°. Of the six stereoscopic
390 pairs at 0-10°, two pairs give satisfactory results on two or three AOIs (mainly Dieppe and
391 Puys). On 23 stereoscopic pairs at 40°, 10 pairs give satisfactory results, mainly on two areas
392 of interest (Varengeville-sur-Mer and Dieppe). Two image pairs have satisfactory 3D
393 reconstruction on the four AOIs: 06/10/2017-06/18/2017 and 06/15/2017-07/06/2017.

394

395 4.3. Identification of radiometric and geometric acquisition parameters favorable for 3D
396 reconstruction of the cliff face

397 Unsurprisingly, the best images for cliff face reconstruction are those with:

- 398 - Sunny weather (e.g. 06/18/2017 and 07/06/2017 in Figures 4 and 5);
- 399 - Few shadows on the cliff face.

400 Both parameters are relevant for a satisfactory tie point detection because they provide various
401 radiometric information. Over the four AOIs, the average radiometry of images which give
402 satisfactory 3D reconstruction is between 300 and 400, whereas the standard deviation is
403 between 80 and 94. This corresponds to a favorable ratio « mean/standard deviation » inferior
404 to 5.

405 The main problem encountered in the 3D reconstruction is the cast shadow phenomenon on
406 the cliff face (umbra and penumbra) that causes the partial or total loss of radiometric
407 information (Arévalo et al., 2006). The summer season is the best period to limit this
408 phenomenon, although it cannot be totally avoided because of the north-facing cliff along the
409 studied coastline. Our current results mean that summer acquisitions are the most appropriate
410 whereas a high temporal frequency is needed by scientists (from daily to seasonal surveys).
411 In recent years several techniques have been studied to detect shadow areas and to
412 compensate the loss of radiometric information or reconstruct it (for a review Shahtahmassebi
413 et al., 2013; Al-Helaly and Muhsin, 2017). Shadow detection methods (thresholding, modeling,
414 invariant color model, shade relief), and de-shadowing methods (e.g. visual analysis,
415 mathematical models, fusion and data mining techniques) will be tested to improve radiometric
416 information for better tie point detection and so higher quality 3D reconstruction.

417 For the geometric acquisition parameters, satisfactory reconstruction also comes from
418 stereoscopic pairs at 0-10° but, with ERDAS IMAGINE®, the cliff face sampling distance is less
419 satisfactory than for reconstruction from 40° stereoscopic pairs. However, the shortest distance
420 between satellite/cliff face at 0-10° incidence angle than at 40° is prone to limited cloud cover.
421 It may therefore be interesting to find a compromise between the incidence angle of images
422 (from 10° to 40°) and the cliff face ground sampling. 3D cliff face reconstructions made by UAV
423 images on the same study area show that 20°, 30° and 40° off-nadir imaging angles provide
424 satisfactory results in terms of accuracy and texture restitution (Jaud et al., 2019). Therefore,
425 a compromise with an angle of incidence of 20° seems promising and will be tested.
426 Furthermore, because of the radiometric variations (different illumination conditions) and

427 geometric ones (in across-track direction) in multi-date stereoscopic pairs with the same
428 incidence angle, it would be interesting to test 3D reconstruction from pairs of images acquired
429 the same day at 0-10° and 40° (same radiometric configuration, but geometric variations in
430 along-track direction).

431

432 4.4. Identification of site parameters most suitable for 3D reconstruction of the cliff face

433 The best reconstructed cliff faces are those in Dieppe and Varengeville-sur-Mer with 10
434 satisfactory 3D reconstructions (Table 6). This can be explained by the highest depths of
435 incision (75 m at Dieppe and 115 m at Varengeville-sur-Mer) and the variability of the cliff face
436 color (high standard deviations in radiometry, 103 and 124 at Varengeville-sur-Mer and Dieppe
437 respectively) which allow easy detection of tie points due to texture change (Figure 4).

438

439 5. Conclusions

440 In this exploratory research, the potential of Pléiades satellite images to monitor coastal cliff
441 face was investigated. The study area in Normandy (from Quiberville to Berneval-le-Grand) is
442 particularly challenging because of its orientation (north-oriented cliff face) and the high
443 frequency of cloud cover. To obtain images with high angle of incidence of the cliff face, a
444 multi-date acquisition was specifically designed. The images with a high angle of incidence
445 (from nadir to 40°) were processed using ASP® and ERDAS IMAGINE®. Interesting 3D
446 reconstructions are obtained, especially with ERDAS IMAGINE® which provides more precise
447 reconstructed points than ASP® (average relative distance and standard deviation of 0.31 m ±
448 2.53 and 0.39 m ± 4.24 respectively) and better distributed over the cliff face providing a
449 reliable dataset. In our study, a minimum of 1 pt/15 m allows visibility of structural
450 discontinuities from the cliff foot to the cliff top. Most of the satisfactory 3D point clouds come
451 from stereoscopic pairs at 40° incidence angle and acquired in summer. The quality of 3D
452 reconstruction of the cliff face mainly depends on radiometric quality, which is better with few
453 cliff shadows and no cloud cover. Sites with deep incisions and cliff face color variability
454 produce the best 3D reconstructions (Varengeville-sur-Mer and Dieppe). The potential of
455 Pléiades images with high angle of incidence is interesting for 3D cliff face reconstruction in
456 the study area if images are acquired in the summer. Because a high angle of incidence can
457 be difficult to obtain from an image supplier, limiting the angle of incidence to about 20° may
458 be a good compromise between the geometry of acquisition and the probability of cloud-free
459 acquisition. This exploratory work creates numerous research opportunities. Seven prospects
460 with Pléiades images will be tested soon: (1) 3D reconstruction with other software (e.g.
461 MicMac®, S2P®, ENVI®) (2) de-shadowing methods over the Norman image dataset (3) multi-
462 date tri-stereo reconstructions (4) a new approach to optimize 3D reconstruction on cliff face
463 on specific areas where change is detected (5) 3D reconstruction from images acquired at the
464 same date with both incidence angle (0-10° and 40°) (6) calculations of retreat distances and
465 eroded volumes when the time interval between images is over 5 years (7) a new area with
466 limited cloud cover, south-facing cliffs and images with an angle of incidence of 20°. For such
467 applications, accurate detection and quantification of cliff face erosion require both a very high
468 resolution and a pointing agility. Currently, WorldView (1 to 4) and Pléiades (1A and 1B) are
469 the imagery satellites which best meet these needs, offering panchromatic Ground Sample
470 Distance (GSD) lower or equal to 50 cm and pointing capability up to +/- 40°. The launching of
471 Pléiades Neo constellation between 2020 and 2022 will also offer new opportunity.

472

473 Acknowledgments

474 The authors acknowledge financial support provided by the TOSCA project EROFALITT from
475 the CNES (the French space agency). This work was also supported by ISblue project,
476 Interdisciplinary graduate school for the blue planet (ANR-17-EURE-0015) and co-funded by
477 a grant from the French government under the program "Investissements d'Avenir". This work
478 was also supported by the ANR project "RICOCHET: multi-risk assessment on coastal territory
479 in a global change context" funded by the French Research National Agency [ANR-16-CE03-
480 0008]. This work is also part of the Service National d'Observation DYNALIT, via the research
481 infrastructure ILICO.

482 The authors thank Scott McMichael, David Shean and Oleg Alexandrov, developers of the
483 ASP® software at NASA, for quickly answering all questions about this software.

484 The Pléiades images are subject to copyright: Pléiades© CNES, Distribution Astrium Services.

485

486 References

487 AIRBUS, 2015. Coastline Changes and Satellite Images Storms over La Salie Beach, French
488 Atlantic Coast (Geo Reportage). AIRBUS Defence & Space.

489 Al-Helaly, E.A., Muhsin, I.J., 2017. A Review: Shadow Treatments and Uses Researches in
490 Satellite Images. *J. Kufa-Phys.* 9, 20–31.

491 Almeida, L.P., Almar, R., Bergsma, E.W.J., Berthier, E., Baptista, P., Garel, E., Dada, O.A.,
492 Alves, B., 2019. Deriving High Spatial-Resolution Coastal Topography From Sub-
493 meter Satellite Stereo Imagery. *Remote Sens.* 11, 590.

494 <https://doi.org/10.3390/rs11050590>

495 Arévalo, V., González, J., Valdes, J., Ambrosio, G., 2006. Detecting shadows in QuickBird
496 satellite images, in: ISPRS Commission VII Mid-Term Symposium" Remote Sensing:
497 From Pixels to Processes", Enschede, the Netherlands. Citeseer, pp. 8–11.

498 ASTRIUM, 2012. Pléiades Imagery - User Guide (Technical report No. USRPHR-DT-125-
499 SPOT-2.0).

500 Berthier, E., Vincent, C., Magnússon, E., Gunnlaugsson, á. þ., Pitte, P., Le Meur, E.,
501 Masiokas, M., Ruiz, L., Pálsson, F., Belart, J.M.C., Wagnon, P., 2014. Glacier
502 topography and elevation changes derived from Pléiades sub-meter stereo images.
503 *The Cryosphere* 8, 2275–2291. <https://doi.org/10.5194/tc-8-2275-2014>

504 Boak, E.H., Turner, I.L., 2005. Shoreline definition and detection: A review. *J. Coast. Res.*
505 21, 688–703. <https://doi.org/10.2112/03-0071.1>

506 Boissin, M.B., Gleyzes, A., Tinel, C., 2012. The pléiades system and data distribution, in:
507 2012 IEEE International Geoscience and Remote Sensing Symposium. Presented at
508 the 2012 IEEE International Geoscience and Remote Sensing Symposium, pp. 7098–
509 7101. <https://doi.org/10.1109/IGARSS.2012.6352027>

510 Collin, A., Hench, J.L., Pastol, Y., Planes, S., Thiault, L., Schmitt, R.J., Holbrook, S.J.,
511 Davies, N., Troyer, M., 2018. High resolution topobathymetry using a Pleiades-1
512 triplet: Moorea Island in 3D. *Remote Sens. Environ.* 208, 109–119.
513 <https://doi.org/10.1016/j.rse.2018.02.015>

514 de Franchis, C., Meinhardt-Llopis, E., Michel, J., Morel, J.-M., Facciolo, G., 2014a. Automatic
515 digital surface model generation from Pléiades stereo images. *Rev. Fr.*
516 *Photogrammétrie Télédétection* 137–142.

517 de Franchis, C., Meinhardt-Llopis, E., Michel, J., Morel, J.-M., Facciolo, G., 2014b. On
518 stereo-rectification of pushbroom images, in: Image Processing (ICIP), 2014 IEEE
519 International Conference On. IEEE, pp. 5447–5451.

520 Gardel, A., Gratiot, N., 2006. Monitoring of coastal dynamics in French Guiana from 16 years
521 of SPOT satellite images. *J. Coast. Res.* 1502–1505.

522 James, M.R., Robson, S., 2012. Straightforward reconstruction of 3D surfaces and
523 topography with a camera: Accuracy and geoscience application. *J. Geophys. Res.*
524 *Earth Surf.* 117. <https://doi.org/10.1029/2011JF002289>

525 Jaud, M., Letortu, P., Théry, C., Grandjean, P., Costa, S., Maquaire, O., Davidson, R., Le
526 Dantec, N., 2019. UAV survey of a coastal cliff face - Selection of the best imaging
527 angle. *Measurement* 139, 10–20. <https://doi.org/10.1016/j.measurement.2019.02.024>

528 Kennedy, D.M., Stephenson, W.J., Naylor, L.A., 2014. Rock coast geomorphology: A global
529 synthesis, Geological Society. ed. Kennedy D.M., Stephenson W.J. and Naylor L.A.,
530 London.

531 Kotov, A.P., Goshin, Y.V., Gavrilov, A.V., Fursov, V.A., 2017. DEM generation based on
532 RPC model using relative conforming estimate criterion. *Procedia Eng.* 201, 708–717.

533 Letortu, P., Costa, S., Bensaid, A., Cador, J.-M., Quénot, H., 2014. Vitesses et modalités de
534 recul des falaises crayeuses de Haute-Normandie (France): méthodologie et
535 variabilité du recul. *Geomorphol. Relief Process. Environ.* 20, 133–144.
536 <https://doi.org/10.4000/geomorphologie.10872>

537 Letortu, P., Costa, S., Maquaire, O., Davidson, R., 2019. Marine and subaerial controls of
538 coastal chalk cliff erosion in Normandy (France) based on a 7-year laser scanner
539 monitoring. *Geomorphology* 335, 76–91.
540 <https://doi.org/10.1016/j.geomorph.2019.03.005>

541 Letortu, P., Jaud, M., Grandjean, P., Ammann, J., Costa, S., Maquaire, O., Davidson, R., Le
542 Dantec, N., Delacourt, C., 2018. Examining high-resolution survey methods for
543 monitoring cliff erosion at an operational scale. *GIScience Remote Sens.* 55, 457–
544 476. <https://doi.org/10.1080/15481603.2017.1408931>

545 Lim, M., Petley, D.N., Rosser, N.J., Allison, R.J., Long, A.J., Pybus, D., 2005. Combined
546 digital photogrammetry and time-of-flight laser scanning for monitoring cliff evolution.
547 *Photogramm. Rec.* 20, 109–129. <https://doi.org/10.1111/j.1477-9730.2005.00315.x>

548 Michoud, C., Carrea, D., Costa, S., Derron, M.H., Jaboyedoff, M., Delacourt, C., Maquaire,
549 O., Letortu, P., Davidson, R., 2014. Landslide detection and monitoring capability of
550 boat-based mobile laser scanning along Dieppe coastal cliffs, Normandy. *Landslides*
551 12, 403–418. <https://doi.org/10.1007/s10346-014-0542-5>

552 Mortimore, R.N., Stone, K.J., Lawrence, J., Duperret, A., 2004. Chalk physical properties and
553 cliff instability, in: *Coastal Chalk Cliff Instability*, Geological Society Engineering
554 Geology Special Publication. pp. 75–88.

555 Moses, C., Robinson, D., 2011. Chalk coast dynamics: Implications for understanding rock
556 coast evolution. *Earth-Sci. Rev.* 109, 63–73.
557 <https://doi.org/10.1016/j.earscirev.2011.08.003>

558 NASA, 2019. The Ames Stereo Pipeline: NASA's Open Source Automated Stereogrammetry
559 Software (No. Version 2.6.2). NASA.

560 Naylor, L.A., Stephenson, W.J., Trenhaile, A.S., 2010. Rock coast geomorphology: Recent
561 advances and future research directions. *Geomorphology* 114, 3–11.
562 <https://doi.org/10.1016/j.geomorph.2009.02.004>

563 Neumann, B., Vafeidis, A.T., Zimmermann, J., Nicholls, R.J., 2015. Future Coastal
564 Population Growth and Exposure to Sea-Level Rise and Coastal Flooding - A Global
565 Assessment. *PLOS ONE* 10, e0118571.
566 <https://doi.org/10.1371/journal.pone.0118571>

567 Pédelaborde, P., 1958. *Le climat du Bassin Parisien : essai d'une méthode rationnelle de*
568 *climatologie physique.*

569 Poli, D., Remondino, F., Angiuli, E., Agugiaro, G., 2015. Radiometric and geometric
570 evaluation of GeoEye-1, WorldView-2 and Pléiades-1A stereo images for 3D
571 information extraction. *ISPRS J. Photogramm. Remote Sens.* 100, 35–47.
572 <https://doi.org/10.1016/j.isprsjprs.2014.04.007>

573 Pomerol, B., Bailey, H.W., Monciardini, C., Mortimore, R.N., 1987. Lithostratigraphy and
574 biostratigraphy of the Lewes and Seaford chalks: A link across the Anglo-Paris Basin
575 at the Turonian-Senonian boundary. *Cretac. Res.* 8, 289–304.

576 Rupnik, E., Deseilligny, M.P., Delorme, A., Klinger, Y., 2016. Refined satellite image
577 orientation in the free open-source photogrammetric tools APERO/MICMAC. *ISPRS*
578 *Ann. Photogramm. Remote Sens. Spat. Inf. Sci.* 3, 83.

579 Salvini, R., Anselmi, M., Rindinella, A., Callegari, I., 2004. Quickbird stereo-photogrammetry
580 for geological mapping (Cyrene-Libya), in: Proceedings of the 20th ISPRS Congress.
581 Presented at the ISPRS Congress, Istanbul, Turkey, pp. 1101–1104.

582 Shahtahmassebi, A., Yang, N., Wang, K., Moore, N., Shen, Z., 2013. Review of shadow
583 detection and de-shadowing methods in remote sensing. *Chin. Geogr. Sci.* 23, 403–
584 420.

585 Shean, D.E., Alexandrov, O., Moratto, Z.M., Smith, B.E., Joughin, I.R., Porter, C., Morin, P.,
586 2016. An automated, open-source pipeline for mass production of digital elevation
587 models (DEMs) from very-high-resolution commercial stereo satellite imagery. *ISPRS*
588 *J. Photogramm. Remote Sens.* 116, 101–117.

589 Stumpf, A., Malet, J.-P., Allemand, P., Ulrich, P., 2014. Surface reconstruction and landslide
590 displacement measurements with Pléiades satellite images. *ISPRS J. Photogramm.*
591 *Remote Sens.* 95, 1–12. <https://doi.org/10.1016/j.isprsjprs.2014.05.008>

592 Trzpit, J., 1970. Climat, in: *Atlas de Normandie*. p. 2.

593 Vanderstraete, T., Goossens, R., Ghabour, T.K., 2003. Bathymetric mapping of coral reefs in
594 the Red Sea (Hurghada, Egypt) using Landsat7 ETM+ Data. *Belgeo* 3, 257–268.

595 Westoby, M.J., Lim, M., Hogg, M., Pound, M.J., Dunlop, L., Woodward, J., 2018. Cost-
596 effective erosion monitoring of coastal cliffs. *Coast. Eng.* 138, 152–164.
597 <https://doi.org/10.1016/j.coastaleng.2018.04.008>

598 White, K., El Asmar, H.M., 1999. Monitoring changing position of coastlines using Thematic
599 Mapper imagery, an example from the Nile Delta. *Geomorphology* 29, 93–105.
600 [https://doi.org/10.1016/S0169-555X\(99\)00008-2](https://doi.org/10.1016/S0169-555X(99)00008-2)

601 Young, A.P., 2018. Decadal-scale coastal cliff retreat in southern and central California.
602 *Geomorphology* 300, 164–175. <https://doi.org/10.1016/j.geomorph.2017.10.010>

603 Young, A.P., Carilli, J.E., 2019. Global distribution of coastal cliffs. *Earth Surf. Process.*
604 *Landf.* 44, 1309–1316. <https://doi.org/10.1002/esp.4574>

605